

Mitigating masked pixels in climate-critical datasets

Angelina Agabin^{1*†}, J. Xavier Prochaska^{2,3†}, Peter Cornillon⁴,
Christian E. Buckingham⁵

^{1*}Department of Applied Math, University of California, Santa Cruz,
1156 High St., Santa Cruz, 95064, CA, USA.

^{2*}Department of Ocean Sciences, University of California, Santa Cruz,
1156 High St., Santa Cruz, 95064, CA, USA.

^{3*}Department of Astronomy & Astrophysics, University of California,
Santa Cruz, 1156 High St., Santa Cruz, 95064, CA, USA.

⁴Graduate School of Oceanography, University of Rhode Island, 215
South Ferry Road, Narragansett, 02874, Rhode Island, USA.

⁵School for Marine Science and Technology, University of Massachusetts,
Dartmouth, 836 South Rodney French Blvd., New Bedford, 02747,
Massachusetts, USA.

*Corresponding author(s). E-mail(s): aagabin@ucsc.edu;
Contributing authors: jxp@ucsc.edu; pcornillon@uri.edu;
christian.buckingham@umassd.edu;

†These authors contributed equally to this work.

Abstract

Remote sensing observations of the Earth’s surface are frequently stymied by clouds, water vapour, and aerosols in our atmosphere. These degrade or preclude the measurement of quantities critical to scientific and, hence, societal applications. In this study, we train a natural language processing (NLP) algorithm with high-fidelity ocean simulations in order to accurately reconstruct masked or missing data in sea surface temperature (SST)—i.e. one of 54 essential climate variables identified by the Global Climate Observing System. We demonstrate that the ENKI model repeatedly outperforms previously adopted inpainting techniques by up to an order-of-magnitude in reconstruction error, while displaying high performance even in circumstances where the majority of pixels are masked. Furthermore, experiments on real infrared sensor data with masking fractions

of at least 40% show reconstruction errors of less than the known sensor uncertainty (RMSE $< \sim 0.1$ K). We attribute ENKI’s success to the attentive nature of NLP combined with realistic SST model outputs, an approach that may be extended to other remote sensing variables. This study demonstrates that systems built upon ENKI-or other advanced systems like it–may therefore yield the optimal solution to accurate estimates of otherwise missing or masked parameters in climate-critical datasets sampling a rapidly changing Earth.

Keywords: Sea Surface Temperature, Machine Learning, Masked Autoencoder, Inpainting

1 Introduction

One of the most powerful means to assess fundamental properties of Earth is via remote sensing, satellite-borne observations of its atmosphere, land, and ocean surface. Since the launch of the Television InfraRed Observation Satellite (TIROS) in 1960, the first of the non-military ‘weather satellites’, remote-sensing satellites have offered daily coverage of the globe to monitor our atmosphere. In 1978, the launch of three satellites directed the attention to our oceans, with sensors observing in the visible portion of the electromagnetic (EM) spectrum to measure ocean color for biological applications, in the infrared (IR) range to estimate sea surface temperature (SST), and in the microwave to estimate wind speed, sea surface height and SST. These programs were followed by a large number of internationally launched satellites carrying a broad range of sensors providing improved spatial, temporal and radiometric resolution for terrestrial, oceanographic, meteorological and cryospheric applications.

All satellite-borne sensors observing Earth’s surface or atmosphere sample some portion of the EM spectrum, with the associated EM waves passing through some or all of the atmosphere. The degree to which the signal sampled is affected by the atmosphere is a strong function of the EM wavelength as well as the composition of the atmosphere, with wavelengths from the visible through the thermal infrared (400 nm – 15 μ m) being the most affected. This is also the portion of the spectrum used to sample a wide range of surface parameters, such as land use, vegetation, ocean color, SST, snow cover, etc. Retrieval algorithms are designed to compensate for the atmosphere for many of these parameters, but these algorithms fail if the density of particulates, such as dust or liquid or crystalin water–think clouds–is too large. The pixels for which this occurs are generally flagged and ignored. This results in a gappy field, with the masked regions ranging from single pixels to regions covering tens of thousands of pixels in size. On average, for example, only $\sim 15\%$ of ocean pixels return an acceptable estimate of SST.

This presents difficulties in the analysis of these fields, especially those requiring complete fields. To address such gaps, data from several different sources are often used with objective analysis interpolation programs to produce what are referred to as Level-4 products: gap-free fields (e.g., [1]). Researchers have also introduced a diversity

of algorithms to fill in clouds (see [2] for a review) including methods using interpolation [3], principal component analyses [4, 5], and, most recently, convolutional neural networks [6, 7]. For SST, these methods achieve average root mean square errors of $\approx 0.2 - 0.5$ K and have input requirements ranging from individual images to an extensive time series.

In this manuscript, we introduce a novel approach, inspired by the vision transformer masked autoencoder (ViTMAE) model of [8] to reconstruct masked pixels in satellite-derived fields. Guided by the intuition that (1) natural images (e.g. dogs, landscapes) can be described by a language and therefore analyzed with natural language processing (NLP) techniques and (2) one can frequently recover the sentiment of sentences that are missing words and then predict these words, [8] demonstrated the remarkable effectiveness of ViTMAE to reconstruct masked images. This included images with 75% masked data, a remarkable inference. Central to ViTMAE’s success was its training on a large corpus of unmasked, natural images. And, given the reduced complexity of most remote-sensing data compared to natural images, one may expect even better performance.

In this study, we use the fine-scale ($1/48^\circ$, 90-level) ocean simulation from the Estimating the Circulation and Climate of the Ocean (ECCO) project and referred to as LLC4320 to train an implementation of the ViTMAE. The LLC4320 model simulates ≈ 14 months of the global ocean at a spatial resolution of $\approx 1 - 2$ km with an hourly snapshot of model variables. Its standard output includes SST, and a comparison of the model output with remote sensing data indicates excellent fidelity [9]. We thereby construct ENKI, a ViTMAE model trained on SST ocean model outputs that may then be applied to actual remote sensing data.

We show below that ENKI reconstructs images of SST anomalies (SSTa) far more accurately than conventional inpainting algorithms. We demonstrate that the combination of high-fidelity model output with state-of-the-art artificial intelligence produces the unprecedented ability to predict critical missing data for both climate-critical and commercial applications. Furthermore, the methodology allows for the comprehensive estimation of uncertainty and an assessment of systematics. The combined power of NLP algorithms and realistic model outputs represent a terrific advance for image reconstruction of remote sensing applications.

2 Results

Figure 1 shows the reconstruction of a representative example from the validation dataset for the ENKI model. We refer to the image as a “cutout”; it is a 64×64 pixels section of the ocean model output with a scale of $\approx 144 \times 144$ km². In this case, the model was trained on cutouts characterized by 20% of the pixels being masked ($t_{\%}=20$ model) but applied to a cutout having 30% of its pixels masked ($m_{\%}=30$). Aside from patches along the outer edge of the input image, it is difficult to visually differentiate the reconstructed pixels from the surrounding SSTa values. The greatest difference is 0.19 K and the highest RMSE in a single 4×4 pixel patch is ≈ 0.07 K with an average RMSE of ≈ 0.02 K. As described below, the performance does degrade with higher $m_{\%}$ and/or greater image complexity, but to levels generally less than standard sensor error.

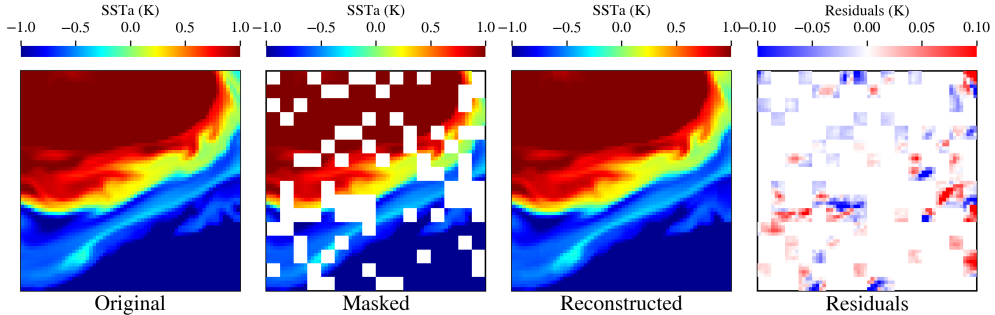


Fig. 1 An example of the ENKI model applied to simulated data with masked or missing pixels. In this case, ENKI was trained on realistic ocean model output consisting of 20% of pixels flagged as “poor” (masked) and applied to an image with 30% of pixels flagged as masked. The panels are: (a) original sea surface temperature anomalies (SSTA), (b) masked SSTA in 4×4 pixels patches covering 20% of the image, (c) reconstructed SSTA, and (d) residual (reconstruction minus truth). Ignoring the image boundary (see Figure 2), the maximum reconstruction error is only ≈ 0.19 K and the highest RMSE in a single patch is ≈ 0.07 K with an average RMSE ≈ 0.02 K.

Quantitatively, we consider first the model performance for individual patches. Figure 2 presents the results of two analyses: (a) the RMSE of reconstruction as a function of the patch spatial location in the image; and (b) the quality of reconstruction as a function of patch complexity, defined by the standard deviation (σ_T) of the patch in the original image. On the first point, it is evident from Figure 2a that ENKI struggles to faithfully reproduce data in patches on the image boundary. This is a natural outcome driven by the absence of data on one or more sides of the patch (i.e., partial extrapolation vs. interpolation). Within this manuscript, we do not include boundary pixels or patches in any quantitative evaluation, and we emphasize that any systems built on a model like ENKI should ignore the boundary pixels in the reconstruction.

Figure 2b, meanwhile, demonstrates that ENKI reconstructs the data with an RMSE that is over one order of magnitude smaller than that anticipated from random chance. Instead, the results track the relation $\text{RMSE} \approx (\sigma_T + 0.014)/9.1$. We speculate that the “floor” in RMSE at $\sigma_T < 10^{-2}$ K arises because of the loss of information in tokenizing the image patches. The nearly linear relation at larger σ_T , however, indicates that the model performance is fractionally invariant with data complexity. We examine these results further in Appendix B.

Turning to performance at the full cutout level, Figure 3a shows results as a function of cutout complexity. For the latter, we adopt a deep-learning metric developed by [3] to identify outliers in SSTA imagery. Their algorithm, named ULMO, calculates a log-likelihood value $LL_{U\text{lmo}}$ designed to assess the probability of a given image occurring within a very large dataset of SST images. [3] and [10] demonstrate that data with the lowest $LL_{U\text{lmo}}$ exhibit greater complexity, both in terms of peak-to-peak temperature anomalies and also in terms of the frequency and strength of fronts, etc.

Figure 3a reveals that the reconstruction performance depends on $LL_{U\text{lmo}}$, with the most complex cutouts showing $\text{RMSE} \approx 0.05 - 0.1$ K. For less complex data

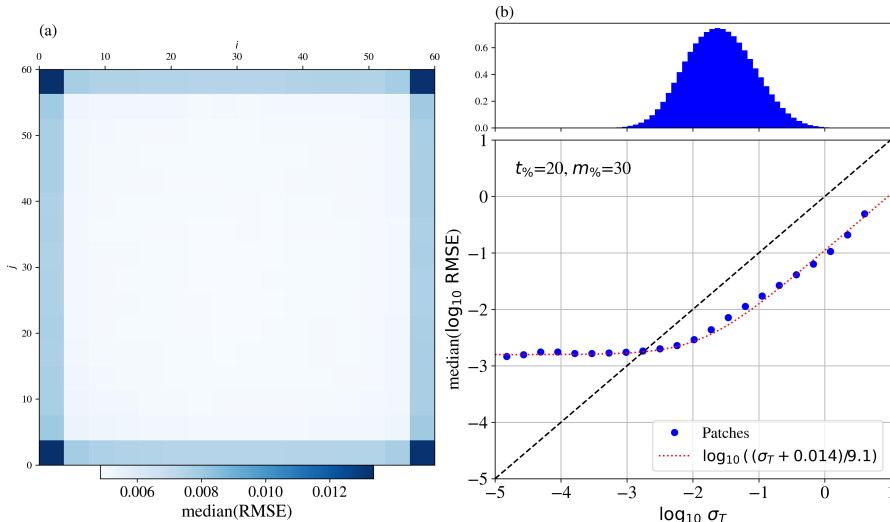


Fig. 2 Results for individual 4×4 pixels patches. Both panels present reconstruction results for the validation dataset using a masking percentile of $m_{\%}=30$ and the $t_{\%}=20$ ENKI model. (a) Median RMSE as a function of the patch spatial location where i, j refers to the position of the lower-left corner of the patch. Patches on the image boundary exhibit systematically higher RMSE and we advocate ignoring these in any image reconstruction application. (b) Median of \log_{10} RMSE for patches as a function of \log_{10} of the standard deviation of SST (σ_T) in the patch. For patches with non-negligible structure ($\sigma_T > 10^{-2}$ K), the reconstruction RMSE is $\approx 10\times$ lower than random (as described by the dashed one-to-one line). The red curve is a two-parameter fit to the data.

($LL_{\text{UImo}} > 200$), the average RMSE < 0.04 K which is effectively negligible for most applications. Even the largest RMSEs are smaller than the sensor errors found by [11] for the pixel-to-pixel noise in SST fields retrieved from the Advanced Very High Resolution Radiometer (AVHRR; $\epsilon_{\text{AVHRR}} \lesssim 0.2$ K), and comparable or better than for the Visible-Infrared Imager-Radiometer Suite (VIIRS; $\epsilon_{\text{VIIRS}} \lesssim 0.1$ K; [11]).

As described in Section 3, we trained ENKI with a range of training mask percentiles expecting best performance with $t_{\%}=75$ as adopted by [8]. Figure 3b shows that for effectively all masking percentiles $m_{\%}$, the $t_{\%}=20$ ENKI model provides best performance. We hypothesize that lower $t_{\%}$ models are optimal for data with lower complexity compared to natural images; i.e., one can sufficiently generalize with $t_{\%} \ll 75\%$. Furthermore, it is evident that models with $t_{\%} > 20$ have not learned the small-scale structure apparent in SST imagery.

For a benchmark test, we compare the results from ENKI against the biharmonic inpainting algorithm (Figure 4). This algorithm was selected because tests have indicated it faithfully reproduces sharp gradients in SST [3]. ENKI outperforms that algorithm by an average factor of $\approx 3\times$ for nearly all of the cutouts except those with negligible structure and very small RMSE (< 0.01 K). These results hold independent of image properties, e.g., image complexity. Moreover, we found similar results hold when comparing with other standard inpainting schemes (see Appendix A).

We have performed a similar benchmark comparison between ENKI and other inpainting algorithms. Appendix A describes results for other interpolation schema

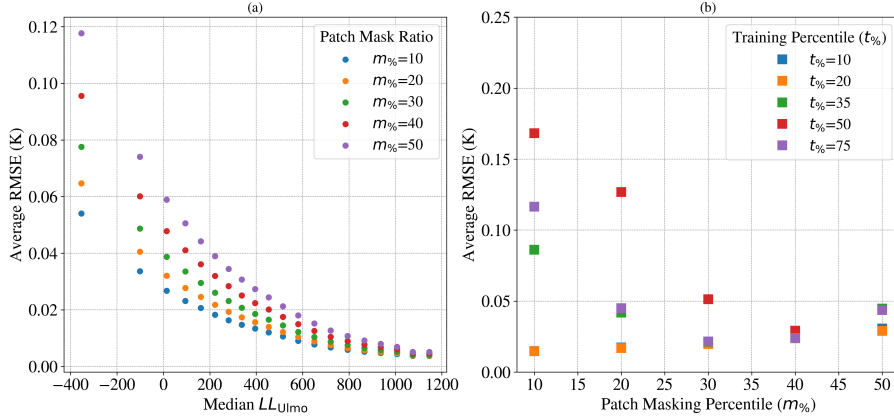


Fig. 3 ENKI’s reconstruction performance on the validation dataset. (a) Model performance as a function of quantiles of image complexity, $LL_{U_{lmo}}$, with higher values indicating lower complexity. The reconstruction error is sensitive to the degree of structure in the field, although for masking percentile $m\% < 20$ even the most complex images have $RMSE \lesssim 0.06$ K. (b) Model performance as a function of masking percentile for the full set of trained ENKI models. Contrary to expectation, we find the $t\%=20$ model outperforms all others at all $m\%$. The poorer performance of the $t\% > 20$ models at low $m\%$ indicates those models have not learned the small-scale features present in SST data.

with results similar (or better, for ENKI) to those presented in Figure 4. In addition, we performed an experiment with one of the most frequently adopted reconstruction techniques for SST observations: the DINEOF algorithm which predicts missing data based on empirical orthogonal function fits to a sequence of masked observations [5]. As detailed in Appendix A, we applied DINEOF to a 180-day sequence of LLC4320 model output with the identical masking implemented in ENKI ($m\%=30$). For an example cutout of $\approx 144 \times 144$ km² in the China Sea, DINEOF yield an average RMSE of ≈ 0.25 K (ignoring the boundary) consistent with published results [5, 6]. In contrast, we find ENKI achieves an average RMSE of ≈ 0.05 K, i.e. a five times improvement. And, we emphasize these are ”one-shot” reconstructions and we have not trained ENKI on a time series nor with geographically limited regions.

As a proof of concept for reconstructing real data, we applied ENKI to the VIIRS dataset described in Section 3. For this exercise, we inserted randomly distributed clouds into cloud-free data, each with a size of 4×4 pixels. Figure 5 shows that the average RMSE values for ENKI are less than sensor error ($RMSE_{VIIRS} < \epsilon_{VIIRS}$) for cutouts with all complexity. The VIIRS reconstructions, however, do show higher average RMSE than those on the LLC4320 validation dataset. A portion of the difference is because the latter does not include sensor noise, which ENKI has (sensibly) not been trained to recreate. We attribute additional error to the fact that the unmasked data also suffers from sensor noise (see Appendix B). And, we also anticipate a portion of the difference is because the VIIRS data have higher spatial resolution than the LLC4320 model. Future experiments with higher resolution models will test this hypothesis.

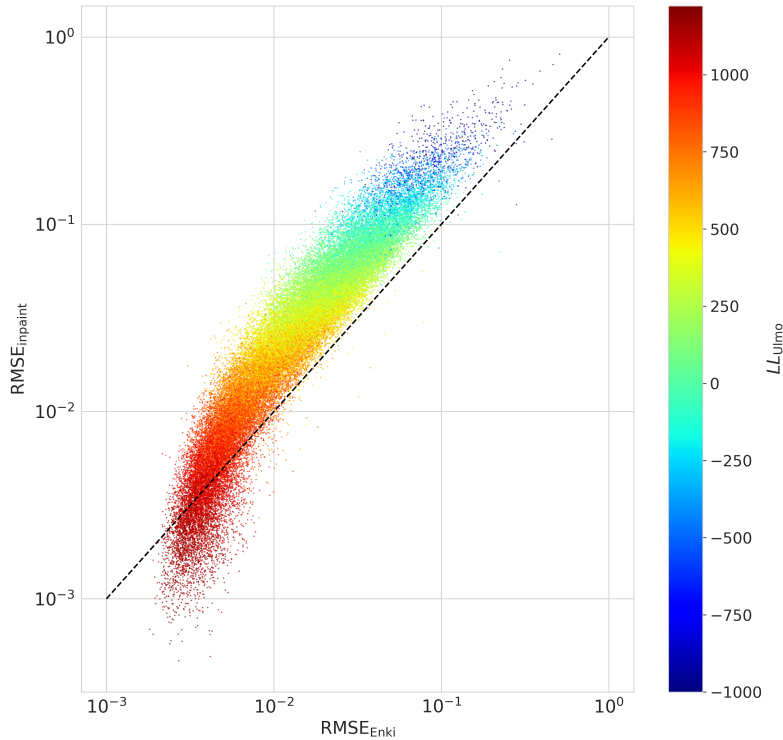


Fig. 4 Comparison of reconstruction error for ENKI ($\text{RMSE}_{\text{ENki}}$) with the biharmonic inpainting algorithm ($\text{RMSE}_{\text{inpaint}}$) on the validation dataset. Colors denote the LL_{Ulmo} metric [3], which is a measure of image complexity; lower values indicate higher image complexity. In $> 99.9\%$ of the cases, ENKI outperforms the inpainting algorithm, and often by more than an order-of-magnitude. This relationship holds independent of the image complexity. The results here correspond to the $t_{\%}=20$ model applied to data with $m_{\%}=30$ masking.

3 Methods

We have designed and trained a machine learning model, inspired by ViTMAE [8], named ENKI to reconstruct masked SST fields [12]. The architecture (Figure 6) inputs (and outputs) a single-channel image, adopts a patch size of 4×4 pixels, and uses 256-dimension latent vectors.

ENKI was trained using SST obtained from ocean model output of the LLC4320. The LLC4320 is a year-long (13 September 2011 to 14 November 2012) global ocean simulation built upon the MITgeneral circulation model [13–15], *i.e.* a primitive equation model that integrates the equations of motion on a $1/48^\circ$ Lat/Lon-Cap (LLC) grid. The simulation is initialized from lower resolution products of the Estimating

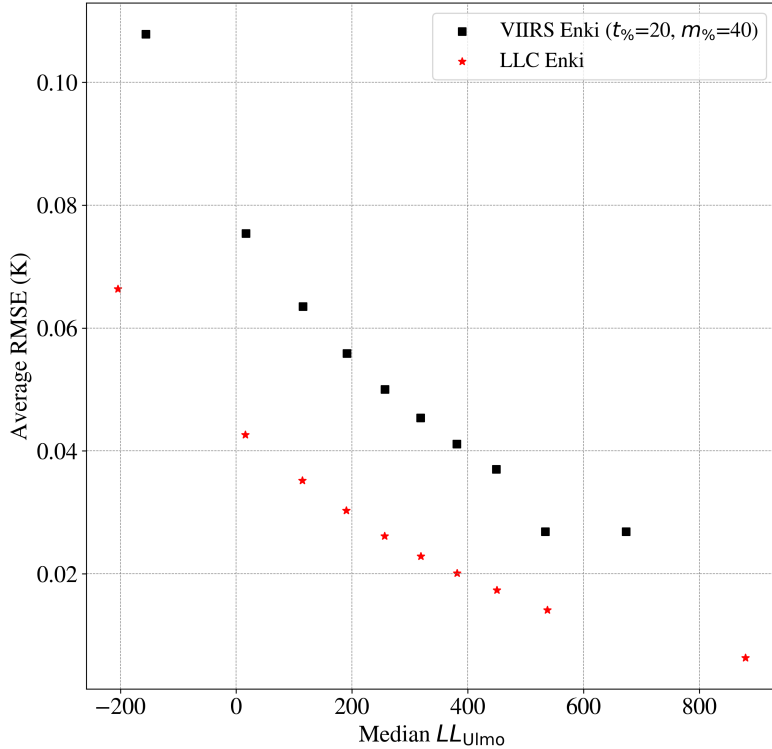


Fig. 5 ENKI performance on real sensor data. The black squares show the average RMSE for reconstructions of VIIRS images in bins of image complexity (higher LL_{Ulmo} indicates less complexity). Even reconstructions of the most complex images ($LL_{Ulmo} < 0$) show the average RMSE is lower than the estimated sensor noise (≈ 0.1 K; [11]). For comparison, we show the average RMSE values for ENKI reconstructions of the LLC4320 validation data (red). All of the results adopt the ENKI model trained with $t_{\%}=20$ and applied to cutouts with $m_{\%}=40$.

the Circulation and Climate of the Ocean (ECCO) project and spun up at progressively higher resolutions. The model is forced at the ocean surface by European Centre for Medium-range Weather Forecasting (ECMWF) reanalysis winds, heat fluxes and precipitation [16], and by barotropic tides [17].

One can, of course, use ‘cloud-free’ portions of SST fields obtained from satellite-borne sensors, however, we often find undetected clouds in these fields, which would impact the training of ENKI. Furthermore, these fields are geographically biased [3] and would yield a highly unbalanced training set.

The LLC4320 simulations have been widely used in a number of studies investigating submesoscale phenomena [18–20], baroclinic tides [17, 21], and mission support for

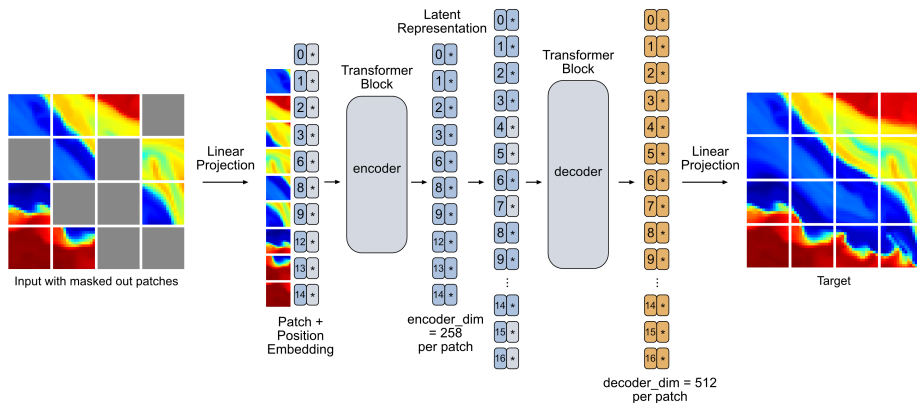


Fig. 6 Architecture of our ViTMAE named ENKI. In this example, the image is 64x64 pixels and broken up into patch sizes of 16x16 pixels with 40% of the image masked out. An image is broken down into patches and masked. The unmasked patches are flattened and embedded by a linear projection with positional embeddings which are then run through the encoder, returning the encoded patches which are then run through the decoder along with the masked (unfilled) tokens. This returns another latent vector, and another linear projection layer outputs this vector as an image with the same dimensions of the original image. The model of ENKI we train reconstructs cutouts of size 64×64 pixels with a patch size of 4×4 pixel² and a latent vector size of 256.

the Surface Water, Ocean Topography (SWOT) satellite sensor [22]. As it has a horizontal grid resolution comparable to but slightly coarser than the spatial resolution of most IR satellite SST measurements, and as it is free from fine-scale atmospheric affects, it represents an oceanographic surface approximately equivalent to but reduced in noise relative to IR satellite SST. See [23] for further details about the implementation of atmospheric effects in the LLC4320. Global model-observation comparisons at these fine horizontal scales can also be found in [9, 24, 25].

Every two weeks beginning 2011-09-13, we uniformly extracted 2,623,152 “cutouts” of $\approx 144 \times 144$ km² from the global ocean at latitudes lower than 57°N, avoiding land. Each of these initial cutouts were re-sized to 64×64 pixels with linear interpolation and mean subtracted. No additional pre-processing was performed.

We constructed a complementary, validation dataset of 655,788 cutouts in a similar fashion. These were drawn from the ocean model on the last day of every 2 months starting 2011-09-30. They were also offset by 0.25 deg in longitude from the spatial locations of the training set.

A primary hyperparameter of the ViTMAE is the training percentage ($t\%$), i.e. the percentage of pixels masked during training (currently a fixed value). While [8] advocates $t\%=75$ to insure generalization, we generated ENKI models with $t\%=[10,20,35,50,75]$. In part, this is because we anticipated applying ENKI to images with less than 50% masked data ($m\% < 50$).

For the results presented here, we train using patches with randomly assigned location (and zero overlap). This is, however, an inaccurate representation of actual

clouds which exhibit spatial correlation on a wide range of scales. Future work will explore how more representative masking affects the results.

ENKI was trained on eight NVIDIA-A10 GPUs on the Nautilus computing system. The most expensive $t_{\%}=10$ model requires 200 hours to complete 400 training epochs with a learning rate of $lr = 10^{-4}$. As described in [12], ENKI exhibits a systematic bias for cases when $m_{\%} \ll t_{\%}$ i.e., mask fractions significantly lower than the training fraction. For the results presented here, we have calculated this bias from the validation dataset and removed it. For the favored model ($t_{\%}=20$), however, this bias term is nearly negligible ($< 10^{-4}$ K).

In addition to the LLC4320 validation dataset, we apply ENKI to actual remote sensing data. These were extracted from the level 2 product of the NOAA processed granules of the VIIRS sensor [26]. We included data from 2012-2021 and only included 64×64 pixels cutouts without any masked data. These are 923,751 cutouts with geographic preference to coastal regions and the equatorial Pacific (see [9]). We caution that while we selected ‘cloud-free’ 64×64 pixels regions, we have reason to believe that a portion of these data are affected by clouds (e.g. [10]).

4 Conclusion

Understanding of the Earth climate system depends heavily upon satellite measurements. In particular, a proper Earth observing system must measure quantities descriptive of the atmosphere, ocean, and land globally and at approximately daily resolution in order to better understand the interaction of these carbon reservoirs with one another. At present, such spatial and temporal coverage is afforded only by space-borne sensors. Moreover, our ability to properly predict these interactions in the future—at least in the short-term—depends strongly upon deductions made using present-day and historical satellite measurements. In summary, remotely-sensed measurements and derived quantities are critical for understanding Earth’s present and future state.

The Global Climate Observing System (GCOS) is a multi-national committee or effort sponsored by the World Meteorological Organization, International Oceanographic Commission, United Nations Environment Programme, and the International Council for Science. Its chief mission is to ensure that observations and information needed to answer climate-relevant questions are obtained and made available to the public. Of the 54 Essential Climate Variables (ECVs) identified by GCOS, it is notable that 8 of these are variables descriptive of the ocean surface, one of these being SST. Moreover, ocean surface heat flux is another closely-related ECV, being heavily determined by SST. Finally, and perhaps more germane to the present discussion, of the 54 ECVs, 26 of these can be measured by satellite sensors that operate in both the visible and infrared portions of the electromagnetic spectrum, with atmospheric conditions (e.g. aerosols, water vapour, and especially clouds) often interfering with these measurements. In fact, only $\sim 15\%$ of the Earth’s surface is visible to these satellite sensors at any given time. It can therefore conservatively be stated that missing or masked pixels due to atmospheric conditions severely limit estimates of 26 of the 54

climate-critical variables. Clearly, these data gaps represent considerable impediments to scientific discovery and, hence, advances in climate prediction.

In this study, we have introduced a new approach (i.e. ENKI) to mitigate missing or masked data through image reconstruction. This dynamically-informed reconstruction technique leverages an NLP algorithm trained on high-fidelity ocean model output to reconstruct masked data in SST fields. We have demonstrated that the ENKI algorithm has reconstruction errors less than approximately 0.1 K for images with up to 50% missing data. That is, the RMSE is comparable or less than typical sensor noise. Furthermore, ENKI outperforms other widely-adopted approaches by up to an order-of-magnitude in RMSE, especially for fields with significant SST structure. Systems built upon ENKI (or perhaps future algorithms like it) may therefore represent an optimal approach to mitigating masked pixels in remote sensing data.

An immediate application of ENKI is the improvement of more than 40 years of SST measurements made by polar-orbiting and geosynchronous spacecraft [12]. In addition to reduction in geographic and seasonal biases [3, 9], improvement of these datasets would likely translate to enhanced time series analysis and teleconnections between ECVs across the globe. One objective of the present work, for example, is the improvement of Level 2 (i.e. swath) SST from the Moderate Resolution Imaging Spectroradiometer (MODIS), a high-resolution (1-km pixels, twice daily) data record which extends from 2000 to the present. Additionally, we anticipate integrating portions of the ENKI encoder within comprehensive deep-learning models (e.g. [27]) in order to predict dynamical processes and extrema at the ocean’s surface.

While manipulation of global, realistic ocean simulations and training on these petabyte-sized datasets offer practical computational and data-storage challenges, the final algorithm is simplistic enough that we expect implementing ENKI within an end-to-end system to reconstruct images for commercial applications would be straightforward. Within this context, enhanced SST measurements would enable improved early detection and monitoring of harmful algal blooms and marine heat-waves [28–30], allowing fisheries and aquaculture industries to take preventative measures and minimize economic losses. At the same time, improved analysis of SST could improve weather forecasts, minimizing risk associated with severe weather events such as tropical cyclones and monsoons [31–33].

Optimal performance of ENKI may be achieved by iterative application of models with a range of $t_{\%}$ and/or trained on specific geographical locations. At the minimum, improvements in the present approach will require models that accommodate a wider range of spatial scales and resolution than has been considered here (e.g. [34]). This is necessary, for example, to accommodate geostationary SST estimates, which have spatial resolutions closer to 5-10 km. We anticipate such improvements are straightforward to implement and are the focus of future work. Finally, we emphasize that the work presented here may be generalized to any remote sensing datasets in which a global corpus of realistic numerical output is available. In the oceanic context, this dataset might be ocean wind vectors, sea surface salinity, ocean color and—with improved biogeochemical modeling—even phytoplankton.

Acknowledgments. We thank David Reiman (Deep Mind) for inspiring this work, and Edwin Goh for his contributions in discussions on hyperparameters and

early results. We also acknowledge use of the Nautilus cloud computing system which is supported by the following US National Science Foundation (NSF) awards: CNS-1456638, CNS1730158, CNS-2100237, CNS-2120019, ACI-1540112, ACI-1541349, OAC-1826967, OAC-2112167.

Appendix A Comparison with Other Approaches

[2] reviews the wide variety of approaches adopted by the community to reconstruct remote sensing data. While a complete comparison to these is beyond the scope of this manuscript, we present additional tests here. Figure A1 shows the results of a series of interpolation schemes adopted in the literature, as a function of cutout complexity gauged by the $LL_{U_{lmo}}$ metric. Of these, the most effective is the biharmonic inpainting algorithm presented in the main text and adopted in our previous works [3]. The figure shows, however, that ENKI outperforms even this method by a factor of $2 - 3\times$ in average RMSE aside from the featureless data ($LL_{U_{lmo}} < 300$).

One of the most widely adopted techniques for remote sensing reconstruction in the literature is the DINEOF algorithm. This approach fits an EOF to a time series of SST data to then predict masked values. We have performed a test of the DINEOF algorithm implemented by [5] and provided as open-source: <https://github.com/aida-alvera/DINEOF>.

Specifically, we analyzed a 180-day sequence of cutouts at lat,lon=118E,21N in the China Sea. Each of these was masked using random 4×4 pixels patches as implemented for ENKI. Figure A2 presents the average RMSE for reconstructions with a range of masking percentiles $m\%$. Similar to published results with DINEOF, we recover an average RMSE of ≈ 0.25 K and independent of $m\%$. In contrast, the ENKI reconstructions have an RMSE ≈ 0.05 , i.e. $\approx 5\times$ lower on average than the DINEOF algorithm. We also emphasize that first results using a convolutional neural network (DINCAE; [6]) yield RMSE values similar to DINEOF. The ViTMAE approach of ENKI offers a qualitative advance over traditional deep-learning vision models.

Appendix B Impacts of sensor and retrieval noise on the performance of ENKI

To better understand the RMSE vs σ_T trends of Fig. 2b and the impacts of noise on ENKI reconstructions of masked areas in SST fields, we decompose both RMSE and σ_T into contributing components.

For satellite-derived SST fields, patch complexity (herein denoted by σ_T) is a function of both (1) noise in the patch resulting from the instrument or noise introduced as part of the retrieval process $\sigma_{noise_o_in}$ and (2) geophysical structure within the field $\sigma_{geo_o_in}$; i.e., the signal of interest in the reconstruction. In these subscripts, the nomenclature “*_o_in*” signifies that these terms relate to the original field and that the σ values correspond to the SST field inside the patch. Reasons for this distinction will become clear below.

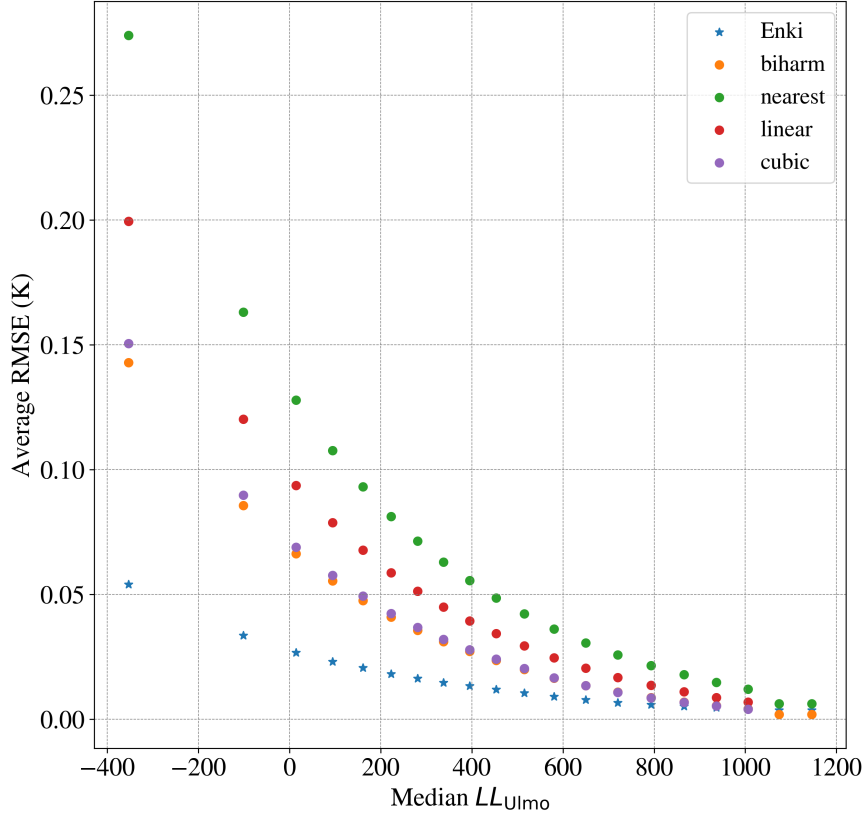


Fig. A1 Comparison of the average RMSE for a series of interpolation schemes (circles) against the results from ENKI. These are for reconstructions of the LLC4320 validation dataset using the $t_{\%}=20$ model on data $m_{\%}=30$ masked patches. Aside from the nearly featureless cutouts ($LL_{Ulmo} > 800$), ENKI well out-performs all of these schema and typically by factors of 3 – 5 \times .

Using these definitions, we can express the signal variance of the patch as

$$\sigma_T^2 = \sigma_{noise_o_in}^2 + \sigma_{geo_o_in}^2 + 2\sigma_{noise_o_in,geo_o_in}^2 \quad (B1)$$

where $\sigma_{geo_o_in}$ is a function of the structure of the field, which we designate as ξ_{o_in} , and $\sigma_{noise_o_in,geo_o_in}^2$ is the covariance between the sensor/retrieval noise and geophysical signal. If we assume negligible correlation between the two sources of variability, then we approximate

$$\sigma_T^2 \approx \sigma_{noise_o_in}^2 + \sigma_{geo_o_in}^2, \quad (B2)$$

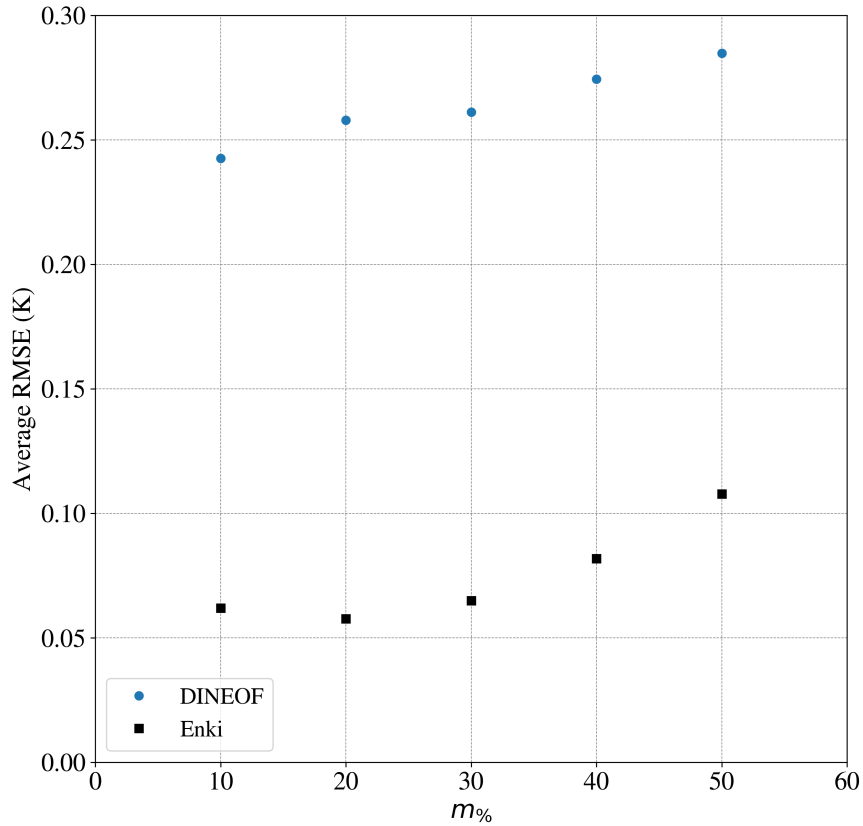


Fig. A2 Average reconstruction error for the DINEOF algorithm (blue circles) applied to 180 days of images from the China Sea. We recover RMSE $\approx 0.25 - 0.3$ K, typical of other published results using DINEOF. Applying the $t\%=20$ ENKI model to the same masked data, we recover an $\approx 5\times$ lower RMSE. We further emphasize that unlike DINEOF does not (yet) incorporate time-series information nor was it trained exclusively on the China Sea.

Moreover, the root mean squared error (RMSE) of the prediction, which constitutes our measure of the quality of the reconstructed image, is given by

$$\text{RMSE}^2(\sigma_{noise_o_in}, \xi_{o_in}, \sigma_{noise_p_in}, \xi_{p_in}) = \sigma_{noise_o_in}^2 + \sigma_{noise_p_in}^2 + f(\xi_{o_in}, \xi_{p_in}) \quad (\text{B3})$$

where the subscript $_p$ references the predicted field, $_o$ refers to the characteristic, either noise or the geophysical signal, outside of the masked areas, and $f(\xi_{o_in}, \xi_{p_in})$ is the contribution to RMSE^2 resulting from the difference between the geophysical

structure of the original field and that of the predicted field in the masked areas. Because ENKI was trained on effectively noise-free model outputs (numerical noise will be negligible), we ignore $\sigma_{noise_p_in}$ hereafter. We also emphasize that the predicted geophysical variability ξ_{p_in} is a function of the noise and geophysical structure in the original field (i.e. outside the masked pixels):

$$\xi_{p_in} = \xi_{p_in}(\sigma_{noise_o_out}, \xi_{o_out}). \quad (\text{B4})$$

While this complex dependence can make interpretation of RMSE vs σ_T curves challenging, we offer the following discussion to aid the reader.

The blue markers in Fig B3 correspond to the noise-free case (i.e., $\sigma_{noise_o_in} = \sigma_{noise_o_out} = 0$):

$$\text{RMSE}^2 = f(\xi_{o_in}, \xi_{p_in}(0, \xi_{o_out})). \quad (\text{B5})$$

In the present context, this corresponds to the case where the original field is model SST. We attribute the flat portion of the curve up to $\sigma_T \approx 10^{-2}$ to two effects. The first is the limited precision of the ViTMAE tokenization of the patches; here we have adopted 256 dimension latent vector. The other effect is a correlation between the size of geophysical structures and the magnitude of σ_T . Specifically, for $\sigma_T \lesssim 0.02$ K the spatial scale of oceanographic features is on the order of or smaller than the 4×4 pixel patch size (i.e. 8×8 km²), such that there is little to no information available to reconstruct the structure in the masked area. As σ_T increases above these values, the spatial scale of the features increases, with more information in the surrounding field available to reconstruct the field within the patch.

But the above analysis and interpretation is free from noise typically encountered in satellite-derived measurements. As previously mentioned, this can occur either due sensor noise or errors due to limitations of the retrieval algorithms used to estimate SST from the measured radiance. To investigate the impact of sensor and retrieval noise on ENKI’s reconstructions, we add 0.04 K white Gaussian noise to the LLC4320 cutouts ($\sigma_{noise_o_in} = \sigma_{noise_o_out} = 0.04$ K in the above nomenclature) giving:

$$\text{RMSE}^2 = (0.04 \text{ K})^2 + f(\xi_{o_in}, \xi_{p_in}(0.04 \text{ K}, \xi_{o_out})) . \quad (\text{B6})$$

We then repeat the analysis. Not surprisingly, the new results (green stars in Fig. B3) follow the 1:1 line up to σ_T of approximately 0.04 K, after which the RMS difference between the masked portions of the reconstructed SST fields and the underlying SST fields, to which 0.04 K Gaussian noise was also added, becomes progressively smaller than σ_T . For $\sigma_T \gtrsim 0.04$ K, the added noise tends to obscure the geophysical structure of the field. As σ_T increases, however, the structure in the field eventually overwhelms the added noise and the improvement in reconstruction approaches that achieved with no noise added—i.e. the blue circles in Fig. B3.

Also shown in Fig. B3 is a similar set of points for VIIRS cutouts, the magenta squares. This curve follows neither the LLC4320 curve without noise (blue circles) nor the LLC4320 curve with noise (green stars). We believe that this results from the non-Gaussian nature of the noise in the VIIRS cutouts. To explore this, we repeat the

above analysis except for $\sigma_{noise_o_in} = 0$ and $\sigma_{noise_o_out} = 0.04$ K; i.e.,

$$RMSE^2 = \sigma_{noise_p_in}^2(0.04 \text{ K}, \xi_{o_out}) + f(\xi_{o_in}, \xi_{p_in}(0.04 \text{ K}, \xi_{o_out})), \quad (B7)$$

which results in the yellow triangles in Fig. B3. The added noise in this case only contributes to RMSE via ENKI’s reconstructed fields; the difference between the blue circles (Eq. B5) and yellow triangles (Eq. B7) is a measure of the impact of the noise added to the region outside of masked areas on ENKI’s reconstructed fields in masked areas. This curve is more similar to the VIIRS curve than the curves for either of the other two cases, no-noise (Eq. B5) or Gaussian noise (Eq. B6), for $10^{-3} \lesssim \sigma_T \lesssim 2 \times 10^{-1}$ K, the range including in excess of 80% of cutouts. This suggests that the noise in the VIIRS fields is not Gaussian. The two primary contributors to non-Gaussian VIIRS noise are (1) *Instrument noise* (VIIRS is a multi-detector instrument and this can introduce noise in the along-track direction at harmonics corresponding to the number of detectors) and (2) *Clouds that were not properly masked by the retrieval algorithm*. Clouds that have not been properly masked tend to result in cold anomalies, often substantially colder than the surrounding cloud-free region, which are structurally incompatible with geophysical processes. Furthermore, such anomalies tend to be relatively small in area—5 to 20 pixels—and in number¹. Although both of these sources of non-Gaussian noise may contribute to the shape of the VIIRS RMSE vs σ_T curve we believe that the primary problem is related to improperly masked clouds or other small scale atmospheric phenomena, which imprint themselves on the SST field as part of the retrieval.

In the above, we have shown how noise in the area surrounding masked pixels affects ENKI’s ability to reconstruct the masked portion of the field. While not a major focus of this work, we have also suggested that non-Gaussian noise in VIIRS SST fields due to clouds, which have not been properly masked, is likely the primary cause of the degradation in ENKI’s ability to reconstruct masked portions of these data.

References

- [1] Reynolds, R.W., Smith, T.M., Liu, C., Chelton, D., Casey, K.S., Schlax, M.G.: Daily high-resolution-blended analyses for sea surface temperature. *Journal of Climate* **20**, 5473–5496 (2007)
- [2] Čatipović, L., Matić, F., Kalinić, H.: Reconstruction methods in oceanographic satellite data observation—a survey. *Journal of Marine Science and Engineering* **11**(2) (2023) <https://doi.org/10.3390/jmse11020340>
- [3] Prochaska, J.X., Cornillon, P.C., Reiman, D.M.: Deep Learning of Sea Surface Temperature Patterns to Identify Ocean Extremes. *Remote Sensing* **13**(4), 744 (2021) <https://doi.org/10.3390/rs13040744> [arXiv:2305.05767](https://arxiv.org/abs/2305.05767) [physics.ao-ph]

¹We have been surprised by the significant fraction of cutouts in the VIIRS, ‘cloud-free’ product we are using that are affected in this fashion.

- [4] Beckers, J.M., Rixen, M.: Eof calculations and data filling from incomplete oceanographic datasets. *Journal of Atmospheric and Oceanic Technology* **20**(12), 1839–1856 (2003) [https://doi.org/10.1175/1520-0426\(2003\)020<1839:ECADFF>2.0.CO;2](https://doi.org/10.1175/1520-0426(2003)020<1839:ECADFF>2.0.CO;2)
- [5] Alvera-Azcárate, A., Barth, A., Rixen, M., Beckers, J.M.: Reconstruction of incomplete oceanographic data sets using empirical orthogonal functions: application to the adriatic sea surface temperature. *Ocean Modelling* **9**(4), 325–346 (2005) <https://doi.org/10.1016/j.ocemod.2004.08.001>
- [6] Barth, A., Alvera-Azcárate, A., Licer, M., Beckers, J.-M.: Dincae 1.0: a convolutional neural network with error estimates to reconstruct sea surface temperature satellite observations. *Geoscientific Model Development* **13**(3), 1609–1622 (2020) <https://doi.org/10.5194/gmd-13-1609-2020>
- [7] Larson, A., Akanda, A.S.: Transforming Observations of Ocean Temperature with a Deep Convolutional Residual Regressive Neural Network (2023)
- [8] He, K., Chen, X., Xie, S., Li, Y., Dollár, P., Girshick, R.B.: Masked autoencoders are scalable vision learners. *CoRR* **abs/2111.06377** (2021) [2111.06377](https://arxiv.org/abs/2111.06377)
- [9] Gallmeier, K., Prochaska, J.X., Cornillon, P.C., Menemenlis, D., Kelm, M.: An evaluation of the LLC4320 global ocean simulation based on the submesoscale structure of modeled sea surface temperature fields. *arXiv e-prints*, 2303–13949 (2023) <https://doi.org/10.48550/arXiv.2303.13949> [arXiv:2303.13949](https://arxiv.org/abs/2303.13949) [physics.ao-ph]
- [10] Prochaska, J.X., Guo, E., Cornillon, P.C., Buckingham, C.E.: The Fundamental Patterns of Sea Surface Temperature. *arXiv e-prints*, 2303–12521 (2023) <https://doi.org/10.48550/arXiv.2303.12521> [arXiv:2303.12521](https://arxiv.org/abs/2303.12521) [physics.ao-ph]
- [11] Wu, F., Cornillon, P., Boussidi, B., Guan, L.: Determining the pixel-to-pixel uncertainty in satellite-derived sst fields. *Remote Sensing* **9**(9) (2017) <https://doi.org/10.3390/rs9090877>
- [12] Agabin, A., Prochaska, J.X.: Reconstructing Sea Surface Temperature Images: A Masked Autoencoder Approach for Cloud Masking and Reconstruction. *arXiv e-prints*, 2306–00835 (2023) <https://doi.org/10.48550/arXiv.2306.00835> [arXiv:2306.00835](https://arxiv.org/abs/2306.00835) [cs.CV]
- [13] Marshall, J., Adcroft, A., Hill, C., Perelman, L., Heisey, C.: A finite-volume, incompressible Navier-Stokes model for studies of the ocean on parallel computers. *J. Geophys. Res.* **102**, 5753–5766 (1997)
- [14] Marshall, J., Hill, C., Perelman, L., Adcroft, A.: Hydrostatic, quasi-hydrostatic, and nonhydrostatic ocean modeling. *J. Geophys. Res.* **102**, 5733–5752 (1997)

- [15] Adcroft, A., Campin, J.-M., Hill, C., Marshall, J.: Implementation of an atmosphere-ocean general circulation model on the expanded spherical cube. *Monthly Weather Review* **132**(12), 2845–2863 (2004) <https://doi.org/10.1175/MWR2823.1>
- [16] Dee, D.P., Uppala, S.M., Simmons, A.J., Berrisford, P., Poli, P., Kobayashi, S., Andrae, U., Balmaseda, M.A., Balsamo, G., Bauer, P., Bechtold, P., Beljaars, A.C.M., Berg, L., Bidlot, J., Bormann, N., Delsol, C., Dragani, R., Fuentes, M., Geer, A.J., Haimberger, L., Healy, S.B., Hersbach, H., Hólm, E.V., Isaksen, I., Kållberg, P., Köhler, M., Matricardi, M., McNally, A.P., Monge-Sanz, B.M., Morcrette, J.-J., Park, B.-K., Peubey, C., Rosnay, P., Tavolato, C., Thépaut, J.-N., Vitart, F.: The ERA-interim reanalysis: configuration and performance of the data assimilation system. *Quarterly Journal of the Royal Meteorological Society* **137**(656), 553–597 (2011) <https://doi.org/10.1002/qj.828>
- [17] Arbic, B.K., Alford, M.H., Ansong, J.K., Buijsman, M.C., Ciotti, R.B., Farrar, J.T.: In: Chassignet, E., Pascual, A., Tintoré, J., Verron, J. (eds.) *A Primer on Global Internal Tide and Internal Gravity Wave Continuum Modeling in HYCOM and MITgcm*. *New Frontiers In Operational Oceanography*, pp. 307–392. GODAE OceanView, FSU, Tallahassee (2018). Chap. 13. <https://doi.org/10.17125/gov2018.ch13>
- [18] Rocha, C.B., Chereskin, T.K., Gille, S.T., Menemenlis, D.: Mesoscale to submesoscale wavenumber spectra in Drake Passage. *Journal of Physical Oceanography* **46**(2), 601–620 (2016)
- [19] Su, Z., Wang, J., Klein, P., Thompson, A.F., Menemenlis, D.: Ocean submesoscales as a key component of the global heat budget. *Nature Communications* **9**(1), 775 (2018). Publisher: Nature Publishing Group
- [20] Torres, H.S., Klein, P., Menemenlis, D., Qiu, B., Su, Z., Wang, J., Chen, S., Fu, L.-L.: Partitioning ocean motions into balanced motions and internal gravity waves: A modeling study in anticipation of future space missions. *J. Geophys. Res.: Oceans* **123**(11), 8084–8105 (2018) <https://doi.org/10.1029/2018JC014438>
- [21] Savage, A.C., Arbic, B.K., Alford, M.H., Ansong, J.K., Farrar, J.T., Menemenlis, D., O’Rourke, A.K., Richman, J.G., Shriver, J.F., Voet, G., Wallcraft, A.J., Zamudio, L.: Spectral decomposition of internal gravity wave sea surface height in global models. *Journal of Geophysical Research: Oceans* **122**(10), 7803–7821 (2017) <https://doi.org/10.1002/2017JC013009>
- [22] Wang, J., Fu, L.-L., Qiu, B., Menemenlis, D., Farrar, J.T., Chao, Y., Thompson, A.F., Flexas, M.M.: An observing system simulation experiment for the calibration and validation of the surface water ocean topography sea surface height measurement using in situ platforms. *Journal of Atmospheric and Oceanic Technology* **35**(2), 281–297 (2018) <https://doi.org/10.1175/JTECH-D-17-0076.1>

- [23] Forget, G., Campin, J.-M., Heimbach, P., Hill, C.N., Ponte, R.M., Wunsch, C.: Ecco version 4: an integrated framework for non-linear inverse modeling and global ocean state estimation. *Geoscientific Model Development* **8**(10), 3071–3104 (2015) <https://doi.org/10.5194/gmd-8-3071-2015>
- [24] Yu, X., Ponte, A.L., Elipot, S., Menemenlis, D., Zaron, E.D., Abernathey, R.: Surface kinetic energy distributions in the global oceans from a high-resolution numerical model and surface drifter observations. *Geophysical Research Letters* **46**(16), 9757–9766 (2019) <https://doi.org/10.1029/2019GL083074>
- [25] Arbic, B.K., Elipot, S., Brasch, J.M., Menemenlis, D., Ponte, A.L., Shriver, J.F., Yu, X., Zaron, E.D., Alford, M.H., Buijsman, M.C., Abernathey, R., Garcia, D., Guan, L., Martin, P.E., Nelson, A.D.: Near-surface oceanic kinetic energy distributions from drifter observations and numerical models. *Journal of Geophysical Research: Oceans* **127**(10), 2022–018551 (2022) <https://doi.org/10.1029/2022JC018551>
- [26] Jonasson, O., Ignatov, A.: Status of second VIIRS reanalysis (RAN2). In: Hou, W.W., Arnone, R.A. (eds.) *Ocean Sensing and Monitoring XI*, vol. 11014, p. 110140. SPIE, ??? (2019). <https://doi.org/10.1117/12.2518908>. International Society for Optics and Photonics
- [27] Tseng, G., Zvonkov, I., Purohit, M., Rolnick, D., Kerner, H.: *Lightweight, Pre-trained Transformers for Remote Sensing Timeseries* (2023)
- [28] Hare, J.A., Alexander, M.A., Fogarty, M.J., Williams, E.H., Scott, J.D.: Forecasting the dynamics of a coastal fishery species using a coupled climate–population model. *Ecological Applications* **20**(2), 452–464 (2010) <https://doi.org/10.1890/08-1863.1>
- [29] Jacox, M.G., Alexander, M.A., Amaya, D., Becker, E., Bograd, S.J., Brodie, S., Hazen, E.L., Pozo Buil, M., Tommasi, D.: Global seasonal forecasts of marine heatwaves. *Nature* **604**(7906), 486–490 (2022) <https://doi.org/10.1038/s41586-022-04573-9>
- [30] Poloczanska, E.S., Brown, C.J., Sydeman, W.J., Kiessling, W., Schoeman, D.S., Moore, P.J., Brander, K., Bruno, J.F., Buckley, L.B., Burrows, M.T., Duarte, C.M., Halpern, B.S., Holding, J., Kappel, C.V., O’Connor, M.I., Pandolfi, J.M., Parmesan, C., Schwing, F., Thompson, S.A., Richardson, A.J.: Global imprint of climate change on marine life. *Nature Climate Change* **3**(10), 919–925 (2013) <https://doi.org/10.1038/nclimate1958>
- [31] Knutson, T.R., Tuleya, R.E.: Impact of CO₂-induced warming on simulated hurricane intensity and precipitation: Sensitivity to the choice of climate model and convective parameterization. *Journal of Climate* **17**(18), 3477–3495 (2004) [https://doi.org/10.1175/1520-0442\(2004\)017<3477:IOCWOS>2.0.CO;2](https://doi.org/10.1175/1520-0442(2004)017<3477:IOCWOS>2.0.CO;2)

- [32] Schade, L.R., Emanuel, K.A.: The ocean's effect on the intensity of tropical cyclones: Results from a simple coupled atmosphere–ocean model. *Journal of the Atmospheric Sciences* **56**(4), 642–651 (1999) [https://doi.org/10.1175/1520-0469\(1999\)056<0642:TOSEOT>2.0.CO;2](https://doi.org/10.1175/1520-0469(1999)056<0642:TOSEOT>2.0.CO;2)
- [33] Sharmila, S., Pillai, P.A., Joseph, S., Roxy, M., Krishna, R.P.M., Chattopadhyay, R., Abhilash, S., Sahai, A.K., Goswami, B.N.: Role of ocean–atmosphere interaction on northward propagation of Indian summer monsoon intra-seasonal oscillations (MISO). *Climate Dynamics* **41**(5), 1651–1669 (2013) <https://doi.org/10.1007/s00382-013-1854-1>
- [34] Reed, C.J., Gupta, R., Li, S., Brockman, S., Funk, C., Clipp, B., Keutzer, K., Candido, S., Uyttendaele, M., Darrell, T.: Scale-MAE: A Scale-Aware Masked Autoencoder for Multiscale Geospatial Representation Learning (2023)

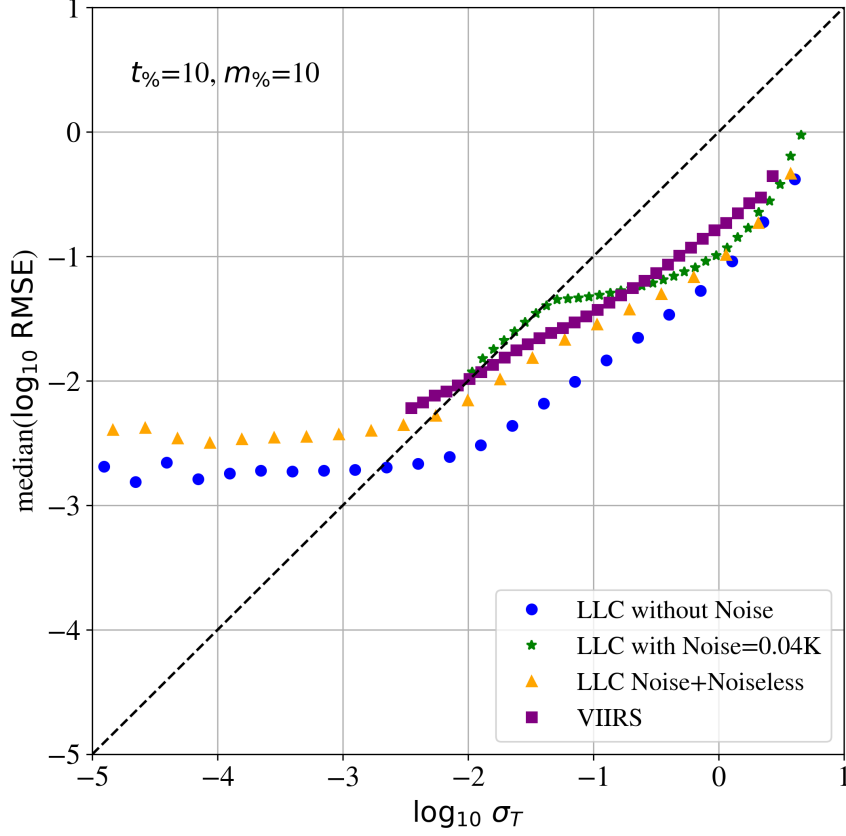


Fig. B3 Investigation of the reconstruction error in individual 4×4 pixels patches as a function of σ_T the measured standard deviation within the patch. For all of the datasets examined, we adopt the $t_{\%}=10$ ENKI model with $m_{\%}=10$ masking. The blue circles are for the noiseless ($\sigma_{noise_o_in}=\sigma_{noise_o_out}=0$ K) LLC4320 validation dataset similar to Figure 2b. The green stars is the same dataset with but with imputed white noise ($\sigma_{noise_o_in}=\sigma_{noise_o_out}=0.4$ K). This curve follows the one-to-one line for $\sigma_T < \sigma_{noise_o_in}$ as expected and then recovers toward the noiseless case as where the geophysical signal dominates σ_T . The yellow triangles, meanwhile, show results where noise was imputed in the unmasked patches but ignored when measuring RMSE ($\sigma_{noise_o_in}=0$ K, $\sigma_{noise_o_out}=0.4$ K). The difference between this case and the noiseless dataset describe the impact of noise in the unmasked data for reconstruction. Last, the magenta squares show results for the VIIRS dataset. See the text for additional discussion on those results.